

# Environmental Breakdown of Topological Interface States in Armchair Graphene Nanoribbon Heterostructures

David M T Kuo

*Department of Electrical Engineering and Department of Physics,  
National Central University, Chungli, 32001 Taiwan*

(Dated: March 18, 2026)

We theoretically investigate the stability and transport properties of topological interface states (IFs) in 9-7-9 and 15-13-15 armchair graphene nanoribbon heterostructures (AGNRHs) laterally embedded in boron nitride (BN) sheets. Two configurations,  $n$ -BNNR/AGNRH/ $n$ -BNNR and  $n$ -BNNR/AGNRH/ $n$ -NBNNR, corresponding to same-topology and reverse-topology BN environments, are examined within a tight-binding framework. Using a bulk boundary perturbation approach, we show that in BNNR/AGNRH/BNNR the IFs are destroyed by chirality breaking induced by symmetric BN environments at both interfaces. In contrast, the IFs in the reverse-topology structure remain robust against lateral interface interactions from BN atoms. Transport calculations further demonstrate that the surviving IFs in BNNR/AGNRH/NBNNR exhibit the characteristic behavior of topological double quantum dots, with an enhanced interdot hopping strength compared with vacuum boundary conditions. These results reveal that BN environments can either suppress or reinforce topological interface states, depending critically on the topology of the surrounding nanoribbons.

## I. INTRODUCTION

Bottom-up synthesis techniques enable the fabrication of graphene nanoribbons (GNRs) with atomic precision [1–10]. Compared with zigzag GNRs (ZGNRs), armchair GNRs (AGNRs) exhibit tunable electronic phases [5], making them promising candidates for nanoelectronic applications [9]. More complex GNR architectures, including 9-7-9 and 7-9-7 armchair graphene nanoribbon heterostructures (AGNRHs) [10] and Janus GNR segments [11], have also been experimentally realized. Scanning tunneling microscopy measurements have confirmed the presence of topological states (TSs) in these systems, such as end states (ESs) and interface states (IFs) in 9-7-9 and 7-9-7 AGNRHs [10].

Although topological IFs in AGNRHs, such as 9-7-9 ribbons, have been extensively studied in idealized or substrate-agnostic models [10,12,13], the role of the environment particularly lateral embedding materials that break sublattice symmetry remains largely unexplored. In realistic device configurations, AGNRHs are inevitably coupled to surrounding materials, raising a critical question: are topological interface states robust against such environmental perturbations? Here, we theoretically investigate a 9-7-9 AGNRH laterally embedded in boron nitride nanoribbons (BNNRs), as illustrated in Fig. 1(a) and 1(b). Two distinct configurations are considered, in which the upper and lower BNNRs realize either the same-topology or reverse-topology scenario. Owing to the difficulty of employing density functional theory (DFT) to compute transmission coefficients in large 9-7-9-AGNRH/BNNR junctions [14–16], we adopt a tight-binding model combined with the Green function technique to evaluate quantum transport in AGNRHs embedded in BN environments [17,18].

Surprisingly, we find that BNNR/AGNRH/NBNNR structures with reverse topology preserve the function-

ality of topological double quantum dots (TDQDs), in which a single energy level associated with each quantum dot remains well isolated from the bulk states. Moreover, the electron hopping strength between the TDQDs is significantly enhanced compared with the vacuum boundary condition. This behavior is highly unusual when contrasted with conventional semiconductor DQD systems [19–26], whose operation is typically restricted to ultra-low temperatures due to the small energy separation between bound and continuum states. Nanoelectronic devices based on TDQDs therefore offer a promising route toward robust high-temperature quantum functionality.

## II. CALCULATION METHODOLOGY

To investigate the transport properties of the BNNR/AGNRH/NBNNR heterojunction connected to metallic electrodes, we employ a combination of a tight-binding model and the Green's function technique [17]. The system Hamiltonian, illustrated in Fig. 1(b), is written as  $H = H_0 + H_{GNR}$ , where  $H_0$  describes the electrodes and their coupling to the nanoribbon system, and  $H_{GNR}$  represents the BNNR/AGNRH/NBNNR structure.

$$H_0 = \sum_k \epsilon_k a_k^\dagger a_k + \sum_k \epsilon_k b_k^\dagger b_k \quad (1)$$

$$+ \sum_\ell \sum_k V_{k,\ell,j}^L d_{\ell,j}^\dagger a_k + \sum_\ell \sum_k V_{k,\ell,j}^R d_{\ell,j}^\dagger b_k + h.c.$$

The first two terms describe free electrons in the left and right metallic electrodes. The operators  $a_k^\dagger$  ( $b_k^\dagger$ ) create an electron with momentum  $k$  and energy  $\epsilon_k$  in the left (right) electrode, respectively. The coupling amplitudes  $V_{k,\ell,j=1}^L$  and  $V_{k,\ell,j=M}^R$  describe tunneling between the left (right) electrode and its adjacent atom located in the  $\ell$ -th row at the zigzag edge.

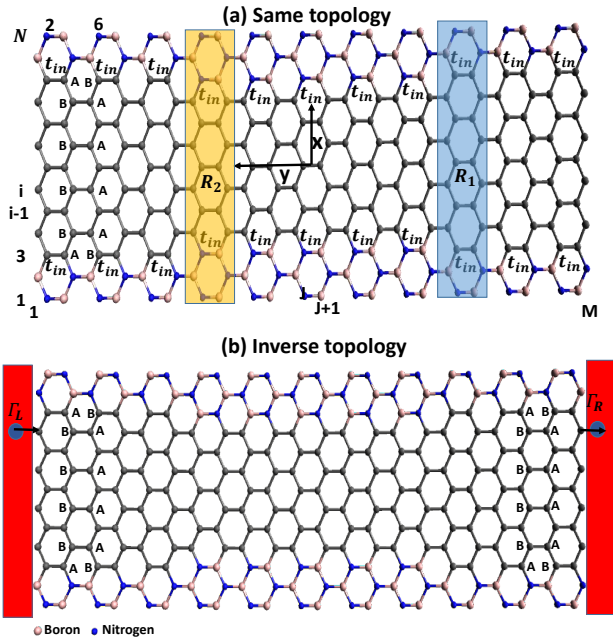


FIG. 1: Schematic illustration of an armchair graphene nanoribbon heterostructure (AGNRH) laterally embedded in a hexagonal boron nitride (BN) sheet, forming two distinct configurations: (a) a same-topology structure, 2-BNNR/9-7-9-AGNRH/2-BNNR, and (b) a reverse-topology structure, 2-BNNR/9-7-9-AGNRH/2-NBNR. White and blue sites denote boron and nitrogen atoms, respectively.  $R_1$  and  $R_2$  represent the unit cells (u.c.) of the 2-BNNR/9-AGNR/2-BNNR and 3-BNNR/7-AGNR/3-BNNR junctions, respectively. The tunable parameter  $t_{in}$  characterizes the interfacial coupling between the AGNRH and the BNNRs. The symbols  $\Gamma_L$  ( $\Gamma_R$ ) represent the electron tunneling rates between the left (right) electrode and the leftmost (rightmost) atoms at the zigzag edges.

$$H_{GNR} = \sum_{\ell,j} E_{\ell,j} d_{\ell,j}^\dagger d_{\ell,j} - \sum_{\ell,j} \sum_{\ell',j'} t_{(\ell,j),(\ell',j')} d_{\ell,j}^\dagger d_{\ell',j'} + h.c. \quad (2)$$

Here,  $E_{\ell,j}$  denotes the on-site energy of the orbital at site  $(\ell, j)$ , while  $d_{\ell,j}^\dagger$  and  $d_{\ell,j}$  are the electron creation and annihilation operators, respectively. The parameter  $t_{(\ell,j),(\ell',j')}$  characterizes the hopping amplitude between sites  $(\ell', j')$  and  $(\ell, j)$ . For the BNNR/AGNRH/NBNR system, we assign on-site energies  $E_B = \Delta_B$ ,  $E_N = -\Delta_N$ , and  $E_C = 0$  for boron, nitrogen, and carbon atoms, respectively. Variations in hopping strengths between different atomic species are neglected, and the condition  $E_B = -E_N = \Delta = 2.7$  eV is adopted for simplicity [27–30]. The nearest-neighbor hopping energy is set to  $t_{(\ell,j),(\ell',j')} = t_{pp\pi} = 2.7$  eV.

To quantify interfacial interactions induced by the BN environment, we introduce an inter-nanoribbon hopping parameter  $t_{in}$  based on bulk boundary perturbation approach[12], as illustrated in Fig. 1(a). When  $t_{in} = 0$ , the BNNR/AGNRH/BNNR (or BNNR/AGNRH/NBNR) structure is decoupled into three isolated segments—the lower BNNR, the central 9-7-9-AGNRH, and the upper BNNR (or NBNR)—each subject to vacuum boundary conditions. Varying  $t_{in}$  effectively models different strengths of lateral interface interactions arising from surrounding two-dimensional insulating environments [31].

The bias-dependent transmission coefficient  $\mathcal{T}_{GNR}(\varepsilon)$  is calculated using  $\mathcal{T}_{GNR}(\varepsilon) = 4Tr[\Gamma_L(\varepsilon)G^r(\varepsilon)\Gamma_R(\varepsilon)G^a(\varepsilon)]$  [13], where  $\Gamma_L(\varepsilon)$  and  $\Gamma_R(\varepsilon)$  denote the tunneling rate (in energy units) at the left and right leads, respectively, and  $G^r(\varepsilon)$  and  $G^a(\varepsilon)$  are the retarded and advanced Green's functions of the GNRs, respectively. In terms of tight-binding orbitals,  $\Gamma_\alpha(\varepsilon)$  and Green's functions are matrices. The expression for  $\Gamma_{L(R)}(\varepsilon)$  is derived from the imaginary part of the self-energies, denoted as  $\Sigma_{L(R)}^r(\varepsilon)$ , and is given by  $\Gamma_{L(R)}(\varepsilon) = -\text{Im}(\Sigma_{L(R)}^r(\varepsilon)) = \pi \sum_k |V_{k,\ell,j=1(M)}^{L(R)}|^2 \delta(\varepsilon - \epsilon_k)$ . In the wide-band limit,  $\Gamma_{L(R)}(\varepsilon)$  is replaced by an energy-independent constant matrix  $\Gamma_{L(R)}$  [12].

### III. RESULTS AND DISCUSSION

Interface-induced modifications of AGNRs embedded in BN sheets have been experimentally observed and shown to alter the band gaps between conduction and valence subbands [32–35]. To elucidate how BN environments affect the topological IFs of 9-7-9-AGNRHs, we first examine the influence of BNNRs with different topologies on individual 7-AGNR and 9-AGNR with  $R_1$  unit cells. Figures 2(a) and 2(b) show the calculated band structures of 4-BNNR/7-AGNR/4-BNNR and 4-BNNR/9-AGNR/4-BNNR, corresponding to same-topology configurations. The resulting band gaps are 1.22 eV and 1.19 eV, respectively, compared with 1.0 eV and 0.9 eV for isolated 7-AGNR and 9-AGNR under vacuum boundary conditions.

For same-topology BN lateral embedding, both the lower and upper BN edges induce sublattice potentials of the same sign. Consequently, the boundary condition imposed by BN resembles that of a vacuum (infinite potential barrier), except that the BN case corresponds to a finite potential barrier. This explains why the band-gap differences between vacuum and BN boundary conditions are relatively small. Indeed, when  $\Delta$  is set to a sufficiently large value (e.g.,  $\Delta = 100$  eV), the two results become nearly indistinguishable. These findings indicate that BN lateral embedding introduces only weak perturbations to the bulk electronic structure when the surrounding BNNRs share the same topology [18,30].

In contrast, for inverse-topology configurations shown in Figs. 2(c) and 2(d), the band gaps of 4-BNNR/7-AGNR/4-NBNR and 4-BNNR/9-AGNR/4-NBNR are significantly reduced to 0.394 eV and 0.454 eV, respectively. This pronounced gap renormalization highlights the strong influence of the BN environment when the lower BNNR has an opposite topology to the upper NBNR. In the inverse-topology case, the sublattice potentials induced at the lower and upper BN edges have opposite signs. Such a boundary condition differs fundamentally from that of AGNRs under vacuum boundary conditions, leading to substantial modifications of the band-edge states.

These tight-binding results are in good agreement with previous DFT calculations [18,30]. The small residual discrepancies suggest that higher-order hopping processes play a negligible role in determining the low-energy conduction and valence subbands. Furthermore, we find that varying the BNNR width ( $n = 6, 8, 10, \dots$ ) does not qualitatively modify the band-edge dispersions, thereby justifying the use of 4-BNNRs in the following analysis.

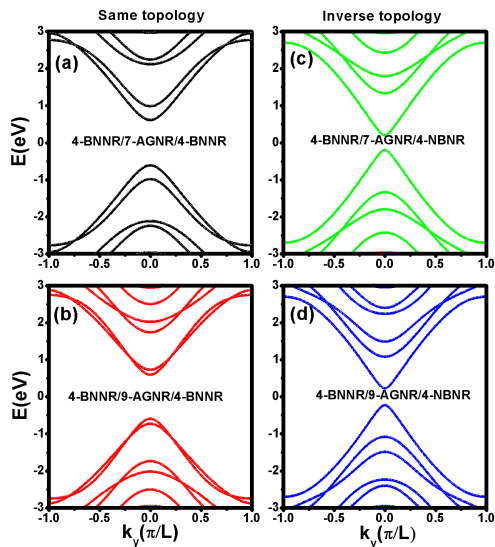


FIG. 2: Quasi-1D electronic band structures of AGNRs embedded in hexagonal BN sheets. Same-topology configurations: (a) 4-BNNR/7-AGNR/4-BNNR and (b) 4-BNNR/9-AGNR/4-BNNR. Inverse-topology configurations: (c) 4-BNNR/7-AGNR/4-NBNR and (d) 4-BNNR/9-AGNR/4-NBNR. We have adopted  $t_{in} = 2.7$  eV and  $\Delta = 2.7$  eV.  $L$  is the length of  $R_1$  unit cell.

In realistic experiments, AGNR and AGNRH segments possess finite lengths, typically below 20 nm[10]. We therefore examine the discrete energy spectra of finite 7-AGNR and 9-7-9 AGNRH segments embedded in BN environments with same and inverse topology, as shown in Fig. 3. Figures 3(a) and 3(b) display the energy levels of 4-BNNR/7-AGNR/4-BNNR and 4-BNNR/9-7-9-

AGNRH/4-BNNR as functions of the interfacial hopping strength  $t_{in}$  for the same-topology case. Due to the finite size of the 4-BNNR/7-AGNR/4-BNNR segment ( $N = 15, M = 80$ ), two in-gap energy levels, denoted as  $\Sigma_{ES,C}$  and  $\Sigma_{ES,V}$ , emerge from the ESs, as shown in Fig. 3(a). In the absence of BN coupling ( $t_{in} = 0$ ), these ESs form near-zero-energy modes. As  $t_{in}$  increases,  $\Sigma_{ES,C}$  and  $\Sigma_{ES,V}$  shift markedly away from zero energy, whereas the bulk-derived states remain largely unchanged. This behavior is consistent with the infinite-length band structures shown in Fig. 2, indicating that BN coupling primarily affects boundary-localized states in the same-topology case.

Figure 3(b) shows four in-gap energy levels originating from two ESs and two IFs in the 9-7-9 AGNRH segment. The IFs arise from the effective end states of the central 7-AGNR segment with  $R_2$  unit cells, as discussed in our previous work [12]. Within the physically relevant range  $0.8 t \leq t_{in} \leq t$ , corresponding to realistic BN coupling strengths, the IF levels  $\Sigma_{IF,C(V)}$  are no longer well isolated from the bulk states. This behavior contrasts sharply with the  $t_{in} = 0$  limit and reflects the enhanced sublattice polarization induced by the symmetric BN environment, which drives the IF levels toward the bulk continuum.

The situation changes dramatically in the inverse-topology configuration shown in Figs. 3(c) and 3(d), where finite 7-AGNR and  $9_6-7_8-9_6$  AGNRH segments are embedded between a BNNR and an NBNR. Although the bulk band gap ( $E_g = E_C - E_V$ ) is substantially reduced for  $0.8 t \leq t_{in} \leq t$ , the energy levels associated with the ESs and IFs in the 9-7-9 AGNRH remain nearly unchanged and well separated from the bulk continuum. Such robustness is highly nontrivial and indicates that the inverse-topology configuration effectively preserves the IFs against strong environmental perturbations.

To clarify the contrasting behaviors observed in Figs. 3(b) and 3(d), we plot the charge densities of  $\Sigma_{IF,C}$  for different  $t_{in}$  values in Fig. 4. Figures 4(a)-4(c) and Figs. 4(d)-4(f) correspond to the inverse-topology and same-topology configurations, respectively. For  $t_{in} = 0$ , shown in Fig. 4(a), the AGNRH is completely decoupled from the BN environment, corresponding to vacuum boundary conditions. The state  $\Sigma_{IF,C}$  originates from the coupling between a 9-7 junction IF state with A-sublattice chirality ( $\Psi_{IF,A}(t_{in} = 0)$ ) and a 7-9 junction IF state with B-sublattice chirality ( $\Psi_{IF,B}(t_{in} = 0)$ ). When a weak coupling  $t_{in} = 0.2 t$  is introduced, the charge density of  $\Sigma_{IF,C}$  partially penetrates into the BN regions [Fig. 4(b)] while preserving mirror symmetry across the ribbon. Even for strong coupling  $t_{in} = 0.8 t$ , as shown in Fig. 4(c),  $\Sigma_{IF,C}$  maintains nearly equal contributions from  $\psi_{IF,A}(t_{in} \neq 0)$  and  $\psi_{IF,B}(t_{in} \neq 0)$ . The charge-density distribution remains mirror-inverted across the ribbon due to the global inversion symmetry of the system. The increased energy separation between  $\Sigma_{IF,C}$  and  $\Sigma_{IF,V}$  is mainly attributed to the enhanced overlap between the wave functions  $\psi_{IF,A}$  and  $\psi_{IF,B}$ . For finite

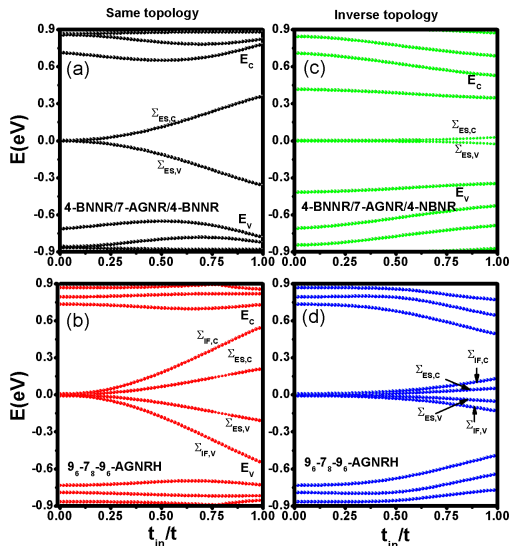


FIG. 3: Energy spectra of finite AGNR (AGNRH) segments as functions of interfacial hopping  $t_{in}$  at  $\Delta = 2.7$  eV. Same-topology scenario: (a) 4-BNNR/7-AGNR/4-BNNR and (b) 4-BNNR/9-7-9-AGNRH/4-BNNR. Inverse-topology scenario: (c) 4-BNNR/7-AGNR/4-NBNR and (d) 4-BNNR/9-7-9-AGNRH/4-NBNR.

$t_{in}$ , the decay lengths of  $\psi_{IF,A}$  and  $\psi_{IF,B}$  increase as a result of interfacial-induced delocalization. Notably, charge densities simultaneously appear on both A- and B-sublattice sites at rows  $i = 5$  and  $i = 13$ , reflecting the symmetric hybridization between the two junction states.

In contrast, Figs. 4(d)-4(f) demonstrate that in the same-topology configuration the IF charge densities become strongly polarized even at  $t_{in} = 0.2 t$ , with dominant contributions from  $\psi_{IF,A}$ . The A(B)-sublattice IF states couple to nitride (boron) atoms at the lower and upper BN edges, respectively, leading to the formation of new bonding and antibonding states [28]. As a result,  $\Sigma_{IF,C(V)}$  shifts above (below) the mid-gap energy. This behavior indicates that the symmetric BN environment generates an effective field along the armchair direction, thereby breaking the inversion symmetry between the 9-7 and 7-9 junctions.

To further elucidate the influence of BN sheets on the IFs shown in Figs. 3 and 4, we introduce an effective Hamiltonian for the IF subspace:

$$H_{eff,IF} = \begin{bmatrix} E_L + \Sigma_A & t_{eff,LR} \\ t_{eff,LR} & E_R + \Sigma_B \end{bmatrix}, \quad (3)$$

where  $E_L = 0$  and  $E_R = 0$  denote the energy levels of the 9-7 and 7-9 junction IF states in the absence of  $t_{in}$ .  $\Sigma_A$  and  $\Sigma_B$  represent the self-energies induced by the interfacial hopping  $t_{in}$ .

For the inverse-topology configuration, the effective Hamiltonian reduces to

$$H_{eff,IF,I} = \begin{bmatrix} 0 & t_{eff,LR} \\ t_{eff,LR} & 0 \end{bmatrix}, \quad (4)$$

since the self-energies satisfy  $\Sigma_{A(B)} = 0$ . More specifically,  $\Sigma_{A(B)} = t_{in}^2 (G_{Bo} + G_{Ni})$ , where  $G_{Bo}$  and  $G_{Ni}$  are the Green's functions describing electron propagation on boron and nitride atoms, respectively. Under the approximation  $\Delta_B = -\Delta_N$ , one has  $G_{Bo} \approx -G_{Ni}$ , leading to nearly vanishing self-energies. In the inverse-topology configuration, the upper BN ribbon is flipped relative to the lower one, reversing the BN sublattice alignment at the two interfaces and restoring chiral symmetry in the IF subspace.

For the same-topology configuration, the effective Hamiltonian becomes

$$H_{eff,IF,S} = \begin{bmatrix} 2\Sigma_{Ni} & t_{eff,LR} \\ t_{eff,LR} & 2\Sigma_{Bo} \end{bmatrix}. \quad (5)$$

In this case, the self-energies satisfy  $\Sigma_{A(B)} = 2\Sigma_{Ni(Bo)}$ , which significantly breaks the chiral symmetry of the IF states. For the same-topology configuration, A sites in graphene couple to the same BN species (nitride atoms) on both sides, while B sites couple to boron atoms on both sides. The resulting asymmetric on-site renormalization explains the polarization of the IF charge densities observed in Fig. 4. The eigenstates of  $H_{eff,IF,I}$  and  $H_{eff,IF,S}$  therefore provide a consistent interpretation of the numerical charge-density distributions.

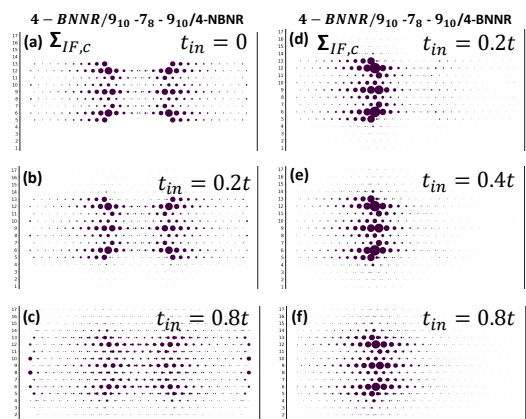


FIG. 4: Charge densities of the interface state  $\Sigma_{IF,C}$  in  $9_{10} - 7_8 - 9_{10}$ -AGNRH embedded in BN at  $\Delta = 2.7$  eV. (a)-(c) Inverse-topology:  $t_{in} = 0$  ( $\Sigma_{IF,C} = 7.53$  meV),  $t_{in} = 0.2 t$  ( $\Sigma_{IF,C} = 8.81$  meV),  $t_{in} = 0.8 t$  ( $\Sigma_{IF,C} = 50.96$  meV). (d)-(f) Same-topology:  $t_{in} = 0.2 t$  ( $\Sigma_{IF,C} = 31.35$  meV),  $t_{in} = 0.4 t$  ( $\Sigma_{IF,C} = 117.57$  meV),  $t_{in} = 0.8 t$  ( $\Sigma_{IF,C} = 0.402$  eV).

Finally, we examine the transport consequences of the robust IFs in inverse-topology structures. Figure 5 presents the calculated transmission coefficient  $\mathcal{T}_{GNR}(\varepsilon)$  for 4-BNNR/9<sub>6</sub>-7<sub>8</sub>-9<sub>6</sub>-AGNRH/4-NBNR at various values of  $t_{in}$ . Pronounced transmission peaks located at  $\Sigma_{IF,C}$  and  $\Sigma_{IF,V}$  confirm that the system effectively operates as a TDQD. In contrast, no distinct transport signatures are observed at the ES-related energy levels, consistent with their short decay lengths relative to the channel length ( $M = 80$ ), which suppresses their coupling to the electrodes [36,37].

The transmission spectra in the vicinity of the IF resonances are well described by  $\mathcal{T}_{TDQD}(\varepsilon) = \frac{4\Gamma_{e,L}t_{eff,LR}^2\Gamma_{e,R}}{|(\varepsilon - E_L + i\Gamma_{e,L})(\varepsilon - E_R + i\Gamma_{e,R}) - t_{eff,LR}^2|}$  in the absence of inter-dot and intra-dot Coulomb interactions [38]. Here,  $\Gamma_{e,L(R)}$  denotes the effective tunneling rate between the electrodes and the left (right) TQD,  $E_{L(R)} = 0$  represent the on-site energies of the two IF states, and  $t_{eff,LR}$  is the effective interdot hopping strength. The zero-temperature electrical conductance is given by  $G_e(\mu) = (2e^2/h)\mathcal{T}_{TDQD}(\varepsilon = \mu)$ , which reaches the conductance quantum  $G_0 = 2e^2/h$  when  $\mu$  aligns with the energy levels  $\Sigma_{IF,C}$  and  $\Sigma_{IF,V}$ . Here,  $\mu$  denotes the Fermi energy of the electrodes.

Notably, the spectra of  $G_e(\mu)$  indicate that the effective hopping  $t_{eff,LR}$  between the IFs in inverse-topology BN environments is enhanced compared with the vacuum boundary condition. This enhancement underscores the constructive role of topology-engineered environments in stabilizing the IFs and strengthening coherent topological transport. In Appendix A, we further investigate the electronic properties of a 15-13-15-AGNRH segment embedded in BN sheets, demonstrating that the above conclusions are not restricted to the 9-7-9 geometry.

#### IV. CONCLUSION

In this work, we theoretically investigated the electronic and transport properties of 9-7-9 and 15-13-15 AGNRHs laterally embedded in boron nitride (BN) sheets. Two sandwich configurations were considered:  $n$ -BNNR/AGNRH/ $n$ -BNNR and  $n$ -BNNR/AGNRH/ $n$ -NBNR, corresponding to same-topology and reverse-topology environments, respectively. These distinct topological configurations give rise to fundamentally different behaviors of the ESs and IFs in the AGNRH.

Within a bulk-boundary perturbation framework, we demonstrate that the topology of the surrounding BN nanoribbons plays a decisive role in determining the stability of the IFs. For same-topology BN environments, interfacial coupling between BN and C atoms induces asymmetric self-energies on the two sublattices. This effect strongly lifts the energy level of the IF state with A-chirality relative to that with B-chirality, breaking the chiral symmetry of the IF subspace and destroying their functionality as TDQDs. As a consequence, the IF levels

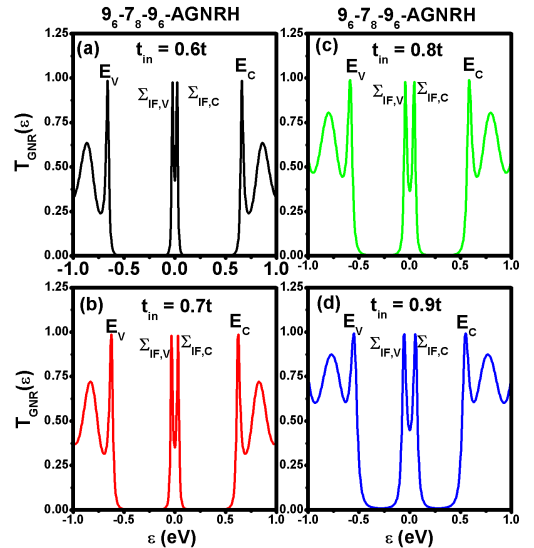


FIG. 5: Transmission coefficients  $\mathcal{T}_{GNR}(\varepsilon)$  of the 4-BNNR/9<sub>6</sub>-7<sub>8</sub>-9<sub>6</sub>-AGNRH/4-NBNR structure for various  $t_{in}$  at  $\Gamma_L = \Gamma_R = \Gamma_t = 2.7$  eV. (a)  $t_{in} = 0.6 t$ , (b)  $t_{in} = 0.7 t$ , (c)  $t_{in} = 0.8 t$ , and (d)  $t_{in} = 0.9 t$ .

hybridize with bulk states and lose their spectral isolation.

In contrast, when the surrounding BN nanoribbons realize a reverse-topology configuration, the global inversion symmetry is restored through mirror-inverted interfaces. In this case, the self-energy corrections from the BN environment largely cancel, leaving the IF energy levels only weakly perturbed. The IFs in  $n$ -BNNR/AGNRH/ $n$ -NBNR therefore remain well separated from the bulk continuum and retain their TDQD functionality, as confirmed by robust resonant transport reaching the conductance quantum.

Our results establish topology-engineered BN environments as an effective route for stabilizing and even enhancing topological interface states in AGNRHs. The demonstrated symmetry-preserved IFs provide a promising platform for realizing robust quantum functionalities in graphene-based nanoelectronic devices, including high-temperature quantum-dot operation[39,40] and qubit-like applications[41-43].

#### Data availability

The data presented in this study are available upon reasonable request.

#### Conflicts of interest

There are no conflicts to declare

## Appendix A: Wider width AGNRHs embedded into boron nitride sheet

In the main text, the electronic properties of two sandwich structures,  $n$ -BNNR/9-7-9-AGNRH/ $n$ -BNNR and  $n$ -BNNR/9-7-9-AGNRH/ $n$ -NBNR, were calculated and analyzed. The former corresponds to a same-topology configuration in which the lower and upper BNNRs share identical topology, whereas the latter represents a reverse-topology configuration. Although only 9-7-9-AGNRH segments have been experimentally synthesized [10], in this appendix we investigate the environmental effects on the transport properties of 15-13-15-AGNRHs in order to examine the size dependence of AGNRH responses to BN embedding.

Figure A.1 presents the calculated energy levels of 4-BNNR/15-13-15-AGNRH/4-BNNR and 4-BNNR/15-13-15-AGNRH/4-NBNR segments as functions of the interfacial hopping strength  $t_{in}$ . The overall trends for the 15-13-15-AGNRH in Fig. A.1 closely resemble those of the 9-7-9-AGNRH shown in Figs. 3(b) and 3(d). However, the bulk band gap of 15-13-15-AGNRH is smaller than that of 9-7-9-AGNRH in both the same-topology and reverse-topology configurations.

In 15-13-15-AGNRHs, six in-gap energy levels appear, consisting of four ESs and two IFs. This follows from the fact that each 15-AGNR segment hosts two left ESs with A-sublattice chirality and two right ESs with B-sublattice chirality. The number of ESs for an  $N$ -AGNR segment with  $R_1$  unit cells is given by  $N_{es} = (N - 3)/6$  and  $N_{es} = (N - 1)/6$  for  $3p$ -width and  $(3p + 1)$ -width AGNRs, respectively. For AGNR segments with  $R_2$  unit cells, the number of ESs becomes  $N_{es} + 1$ . Consequently, the central 13-AGNR segment possesses three ESs at each terminus. The number of IFs at each junction is determined by  $N_{IF} = |N_{es, cen} - N_{es, out}|$ , where  $N_{es, cen}$  and  $N_{es, out}$  denote the numbers of ESs in the central and outer AGNR segments, respectively [12]. At the 15-13 junction, one IF state with A-chirality emerges, whereas at the 13-15 junction one IF state with B-chirality appears.

In the same topology configuration shown in Fig. A.1(a), the energy-level separation  $\Delta_{IF}$  between  $\Sigma_{IF,C}$  and  $\Sigma_{IF,V}$  for  $t_{in} = 0$  originates from the wave-function overlap between the A-chirality and B-chirality IFs. We note that  $\Delta_{IF}$  in 15-13-15-AGNRH segments is substantially larger than that in 9-7-9-AGNRH segments, reflecting stronger intrinsic coupling between the two IFs. When  $t_{in} \leq 0.1 t$ ,  $\Delta_{IF}$  remains nearly unchanged, whereas for  $t_{in} > 0.2 t$ ,  $\Delta_{IF}$  exhibits an approximate  $t_{in}^2$  dependence. This behavior is attributed to the gradual decoupling between the A-chirality and B-chirality IFs as their spatial decay lengths are modified (see Fig. A.2(c)).

In the reverse-topology configuration shown in Fig. A.1(b),  $\Delta_{IF} = 2t_{eff,LR}$  remains nearly constant for  $t_{in} \leq 0.3 t$ . At  $t_{in} = t$ , we obtain  $E_g = 0.9$  eV and  $\Delta_{IF} = 0.362$  eV for the 15<sub>6</sub>-13<sub>8</sub>-15<sub>6</sub>-AGNRH segment, compared with  $E_g = 0.978$  eV and  $\Delta_{IF} = 0.264$  eV

for the 9<sub>6</sub>-7<sub>8</sub>-9<sub>6</sub>-AGNRH segment. According to Eq. (4), the variation of  $\Delta_{IF}$  with respect to  $t_{in}$  is governed by the effective inter-IF coupling  $t_{eff,LR}$ . The results of Fig. A.1(b) therefore indicate that the coherent length of IFs in 15-13-15-AGNRH segments is longer than that in 9-7-9-AGNRH segments, even in the presence of BN embedding.

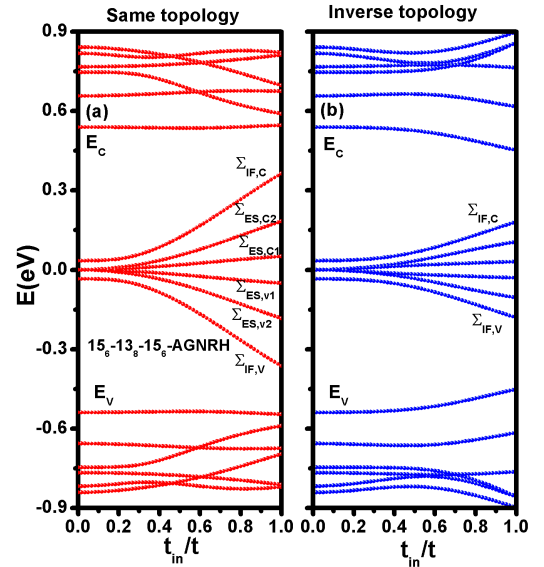


FIG. A.1: Energy spectra of finite 15<sub>6</sub>-13<sub>8</sub>-15<sub>6</sub> AGNRH segments as a function of the interfacial hopping  $t_{in}$  at  $\Delta = 2.7$  eV. (a) Same-topology configuration: 4-BNNR/15<sub>6</sub>-13<sub>8</sub>-15<sub>6</sub>-AGNRH/4-BNNR. (b) Inverse-topology configuration: 4-BNNR/15<sub>6</sub>-13<sub>8</sub>-15<sub>6</sub>-AGNRH/4-NBNR. The spectra illustrate the evolution of end states (ESs) and interface states (IFs) under increasing BN coupling.

In Fig. A.1(a), the energy levels of the topological states are shifted due to the polarization induced by the BN sheets. To further elucidate the polarization effects arising from BNNRs in the same-topology scenario, we plot the charge densities of  $\Sigma_{IF,C}$  for the 15<sub>6</sub>-13<sub>8</sub>-15<sub>6</sub> AGNRH at different interfacial hopping strengths  $t_{in}$  in Fig. A.2. Figures A.2(a)-2(f) correspond to  $t_{in} = 0$ ,  $t_{in} = 0.2 t$ ,  $t_{in} = 0.4 t$ ,  $t_{in} = 0.6 t$ ,  $t_{in} = 0.8 t$ , and  $t_{in} = t$ , respectively. For  $t_{in} = 0$  and  $t_{in} = 0.2 t$ , the charge densities of  $\Sigma_{IF,C}$  are mostly confined within the graphene ribbon. However, even at  $t_{in} = 0.2 t$ , the A-sublattice sites exhibit a noticeable enhancement of charge density, indicating the onset of BN-induced polarization. When  $t_{in} = 0.4 t$ , the charge density becomes predominantly localized on the A-sublattice sites, which reflects the significant self-energy contributions  $\Sigma_{N_i}$  and  $\Sigma_{B_o}$  in Eq. (5).

As  $t_{in}$  increases further to  $0.6 t$ ,  $0.8 t$ , and  $t$ , the charge density of  $\Sigma_{IF,C}$  extends to the B-sublattice sites at the BN edges (corresponding to nitride atom positions). Simultaneously, the B-sublattice sites at rows  $i = 5$  and

$i = 19$  in the left 15-AGNR segment also display enhanced charge density. This indicates a strong coupling between the A- and B-sublattice sites within the left 15-AGNR segment, resulting in a wave-function delocalization of  $\Sigma_{IF,C}$  across the ribbon and into the BN edges.

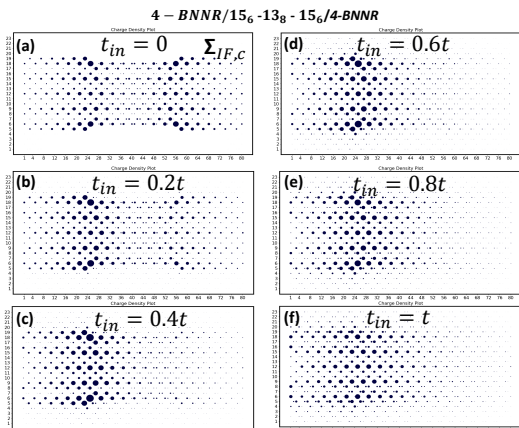


FIG. A.2: Charge density distributions of the interface state  $\Sigma_{IF,C}$  in the 4-BNNR/15<sub>6</sub>-13<sub>8</sub>-15<sub>6</sub>-AGNRH/4-BNNR segment at  $\Delta = 2.7$  eV. Panels (a)-(f) correspond to the same-topology configuration with interfacial hopping  $t_{in} = 0$  ( $\Sigma_{IF,C} = 34.27$  meV),  $0.2t$  ( $\Sigma_{IF,C} = 40.9$  meV),  $0.4t$  ( $\Sigma_{IF,C} = 85.2$  meV),  $0.6t$  ( $\Sigma_{IF,C} = 0.167$  eV),  $0.8t$  ( $\Sigma_{IF,C} = 0.266$  eV), and  $t$  ( $\Sigma_{IF,C} = 0.363$  eV), illustrating the progressive polarization and delocalization of the interface state induced by BN coupling.

To examine the transport properties of the 4-BNNR/15-13-15-AGNRH/4-BNNR segment, we calculate the transmission coefficient  $\mathcal{T}_{GNR}(\varepsilon)$  as a function of applied voltage, which generates a uniform electric field along the negative  $y$ -direction, as shown in Fig. A.3 for interfacial hopping  $t_{in} = 0.8t$  [27–29]. The potential induced by the electric field is incorporated into the system Hamiltonian (Eq. (2)) as  $U_y = -eF_y y$ , where  $F_y = V_y/L_a$ ,  $V_y$  is the applied bias, and  $L_a$  is the length of the AGNRH segment[36,37].

In Fig. A. 3(a) at  $V_y = 0$ , two small transmission peaks labeled  $\Sigma_{IF,C}$  and  $\Sigma_{IF,V}$  appear within the bulk gap. Charge transport through these IF levels can be effectively modeled as a single quantum dot (QD) with one energy level and asymmetric tunneling rates  $\Gamma_{e,L} \neq \Gamma_{e,R}$  [43]. This demonstrates that the IFs in 4-BNNR/15-13-15-AGNRH/4-BNNR behave as a single TQD at zero bias. Increasing the tunneling rates between the zigzag edge structures of the AGNRH and the electrodes, from  $\Gamma_t = 0.56$  eV to 2.7 eV, enhances the peak amplitudes, although  $\mathcal{T}_{GNR}$  remains relatively small due to the asymmetry of  $\Gamma_{e,L}$  and  $\Gamma_{e,R}$ , as suggested by the charge density distribution in Fig. A.2(e). As illustrated

in Figs. A.3(b)-(d), the separation between the  $\Sigma_{IF,C}$  and  $\Sigma_{IF,V}$  peaks decreases as  $V_y$  increases. Notably,  $\mathcal{T}_{GNR}$  reaches unity at  $V_y = 1.215$  V with  $\Gamma_t = 0.56$  eV in Fig. A.3(d). These results indicate that the 4-BNNR/15-13-15-AGNRH/4-BNNR segment undergoes a transition from a single TQD to a TDQD under electric-field modulation. Finally, we would like to point out that our conclusions remain valid even in the case of  $\Delta_B \neq -\Delta_N$ . For example, when the energy level of boron atoms is  $\Delta_B = 2.329$  eV and the energy level of nitride atoms is  $\Delta_N = -2.499$  eV, the band inversion symmetry shown in Fig. A.1 is slightly lifted. However, the transmission coefficient still exhibits the resonant tunneling characteristic associated with topological interface states in the 4-BNNR/AGNRH/4-BNNR configuration.

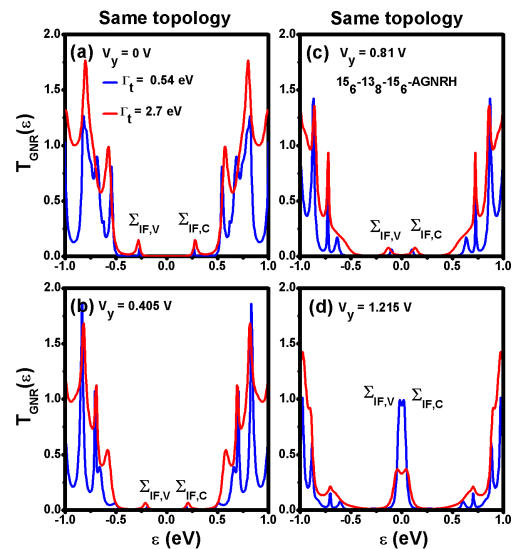


FIG. A.3: Transmission coefficients  $\mathcal{T}_{GNR}(\varepsilon)$  of the 4-BNNR/15<sub>6</sub>-13<sub>8</sub>-15<sub>6</sub>-AGNRH/4-BNNR segment at  $t_{in} = 0.8t$  under various applied voltages  $V_y$ : (a)  $V_y = 0$ , (b)  $V_y = 0.405$  V, (c)  $V_y = 0.81$  V, and (d)  $V_y = 1.215$  V. Blue and red curves correspond to tunneling rates  $\Gamma_L = \Gamma_R = \Gamma_t = 0.56$  eV and  $\Gamma_t = 2.7$  eV, respectively. The panels illustrate the evolution from a single topological quantum dot at zero bias to a topological double quantum dot under electric-field modulation.

### Acknowledgments

This work was supported by the National Science and Technology Council, Taiwan under Contract No. MOST 107-2112-M-008-023MY2.

E-mail address: mtkuo@ee.ncu.edu.tw

<sup>1</sup> J. Cai, P. Ruffieux, R. Jaafar, M. Bieri, T. Braun, S. Blankenburg, M. Muoth, A. P. Seitsonen, M. Saleh, X.

Feng, K. Mullen and R. Fasel, Atomically precise bottom-

- up fabrication of graphene nanoribbons, *Nature*, 2010, **466**, 470.
- <sup>2</sup> J. Z. Liu, B. W. Li, Y. Z. Tan, A. Giannakopoulos, C. Sanchez-Sanchez, D. Beljonne, P. Ruffieux, R. Fasel, X. L. Feng and K. Mullen, Toward Cove-Edged Low Band Gap Graphene Nanoribbons, *J. Am. Chem. Soc.*, 2015, **137**, 6097.
  - <sup>3</sup> Y. C. Chen, T. Cao, C. Chen, Z. Pedramraz, D. Haberer, D. G. de Oteyza, R. Fischer, S. G. Louie and M. F. Crommie, Molecular bandgap engineering of bottom-up synthesized graphene nanoribbon heterojunctions, *Nat. Nanotechnol.*, 2015, **10**, 156.
  - <sup>4</sup> P. Ruffieux, S. Y. Wang, B. Yang, A. Sanchez, J. Liu, T. Dienel, L. Talirz, P. Shinde, C. Pignedoli, D. Passerone, T. Dumslaff, X. L. Feng, K. Mullen and R. Fasel, On-surface synthesis of graphene nanoribbons with zigzag edge topology, *Nature*, 2016, **531**, 489.
  - <sup>5</sup> J. P. Llinas, A. Fairbrother, G. Borin Barin, W. Shi, K. Lee, S. Wu, B. Y. Choi, R. Braganza, J. Lear, N. Kau et al. Short-channel field-effect transistors with 9-atom and 13-atom wide graphene nanoribbons. *Nat. Commun.*, 2017, **8**, 633.
  - <sup>6</sup> P. H. Jacobse, A. Kimouche, T. Gebraad, M. M. Ervasti, J. M. Thijssen, P. Liljeroth, and I. Swart, Electronic components embedded in a single graphene nanoribbon. *Nat Commun.*, 2017, **8**, 119.
  - <sup>7</sup> L. Y. Lee, F. Z. Zhao, T. Cao, I. Jisoon and S. G. Louie, Topological Phases in Cove-Edged and Chevron Graphene Nanoribbons: Geometric Structures,  $Z(2)$  Invariants, and Junction States, *Nano Lett.*, 2018, **18**, 7274.
  - <sup>8</sup> D. J. Rizzo, G. Veber, J. W. Jiang, R. McCurdy, T. Bronner, T. Cao, T. Chen, S. G. Louie, F. R. Fischer and M. F. Crommie, Inducing metallicity in graphene nanoribbons via zero-mode superlattices, *Science*, 2020, **369**, 1597.
  - <sup>9</sup> H. M. Wang, H. S. Wang, C. X. Ma, L. X. Chen, C. X. Jiang, C. Chen, X. M. Xie, A. P. Li and X. R. Wang, Graphene nanoribbons for quantum electronics, *Nat. Rev. Phys.* 2021, **3**, 791.
  - <sup>10</sup> D. J. Rizzo, J. W. Jiang, D. Joshi, G. Veber, C. Bronner, R. A. Durr, P. H. Jacobse, T. Cao, A. Kalayjian, H. Rodriguez, P. Butler, T. Chen, S. G. Louie, F. R. Fischer and M. F. Crommie, Rationally Designed Topological Quantum Dots in Bottom-Up Graphene Nanoribbons, *ACS Nano*, 2021, **15**, 20633.
  - <sup>11</sup> S. T. Song, Y. Teng, W. C. Tang, Z. Xu, Y. Y. He; J. W. Ruan, T. Kojima, W. P. Hu, F. J. Giessibl, H. Sakaguchi, S. G. Louie, and J. Lu, Janus graphene nanoribbons with localized states on a single zigzag edge, *Nature*, 2025, **637**, 580.
  - <sup>12</sup> David M. T. Kuo, Topological Interface States and Non-linear Thermoelectric Performance in Armchair Graphene Nanoribbon Heterostructures, *RSC Adv.*, 2026, **16**, 4680.
  - <sup>13</sup> David M. T. Kuo, Room-Temperature Pauli Spin Blockade and Current Rectification in 15-13-15 Armchair Graphene Nanoribbon Heterostructures, *Nanoscale*, 2025, **17**, 18920.
  - <sup>14</sup> Y. W. Son, M. L. Cohen, and S. G. Louie, Energy Gaps in Graphene Nanoribbons, *Phys. Rev. Lett.*, 2006, **97**, 216803.
  - <sup>15</sup> Y. Matsuda, W. Q. Deng and III W A Goddard, Contact Resistance for "End-Contacted" Metal-Graphene and Metal-Nanotube Interfaces from Quantum Mechanics, *J. Phys. Chem. C*, 2010, **114**, 17845.
  - <sup>16</sup> V. T. Nikita, M. Ruize, L. Johannes, K. Efthimios, A. M. Arash, and P. Michele, Dirac Half-Semimetallicity and Antiferromagnetism in Graphene Nanoribbon/Hexagonal Boron Nitride Heterojunctions, *Nano Lett.*, 2023, **23**, 6698.
  - <sup>17</sup> Z. H. Qiao, J. Jung and A. H. MacDonald, Electronic Highways in Bilayer Graphene, *Nano Lett.*, 2011, **11**, 3453.
  - <sup>18</sup> J. Jung, Z. H. Qiao, Q. Niu, and A. H. MacDonald, Transport Properties of Graphene Nanoroads in Boron Nitride Sheets, *Nano Lett.*, 2012, **12**, 2936.
  - <sup>19</sup> K. Ono, D. G. Austing, Y. Tokura and S. Tarucha, Current Rectification by Pauli Exclusion in a Weakly Coupled Double Quantum Dot System, *Science*, 2002, **297**, 1313.
  - <sup>20</sup> W. G. van der Wiel, S. De Franceschi, J. M. Elzerman, T. Fujisawa, S. Tarucha, and L. P. Kouwenhoven, Electron transport through double quantum dots, *Rev. Mod. Phys.*, 2003, **75**, 1.
  - <sup>21</sup> J. R. Petta, A. C. Johnson, J. M. Taylor, E. A. Laird, A. Yacoby, M. D. Lukin, C. M. Marcus, M. P. Hanson and A. C. Gossard, Coherent manipulation of coupled electron spins in semiconductor quantum dots, *Science*, 2005, **309**, 2180.
  - <sup>22</sup> F. H. L. Koppens, C. Buizert, K. J. Tielrooij, I. T. Vink, K. C. Nowack, T. Meunier, L. P. Kouwenhoven and L. M. K. Vandersypen, Driven coherent oscillations of a single electron spin in a quantum dot, *Nature*, 2006, **442**, 766.
  - <sup>23</sup> B. M. Maune, M. G. Borselli, B. Huang, T. D. Ladd, P. W. Deelman, K. S. Holabird, A. A. Kiselev, I. AlvaradoRodriguez, R. S. Ross, A. E. Schmitz, M. Sokolich, C. A. Watson, M. F. Gyure and A. T. Hunter, Coherent singlet-triplet oscillations in a silicon-based double quantum dot, *Nature*, 2012, **481**, 344.
  - <sup>24</sup> X. J. Hao, R. Ruskov, M. Xiao, C. Tahan and H. W. Jiang, Electron spin resonance and spin-valley physics in a silicon double quantum dot, *Nat. Commun.*, 2014, **5**, 3860.
  - <sup>25</sup> B. Weber, Y. H. M. Tan, S. Mahapatra, T. F. Watson, H. Ryu, R. Rahman, L. C. L. Hollenberg, G. Klimeck and M. Y. Simmons, Spin blockade and exchange in Coulomb-confined silicon double quantum dots, *Nat. Nanotechnol.*, 2014, **9**, 430.
  - <sup>26</sup> D. M. Zajac, A. J. Sigillito, M. Russ, F. Borjans, J. M. Taylor, G. Burkard and J. R. Petta, Resonantly driven CNOT gate for electron spin, *Science*, 2018, **359**, 439.
  - <sup>27</sup> Y. Ding, Y. Wang and J. Ni, Electronic properties of graphene nanoribbons embedded in boron nitride sheets, *Appl. Phys. Lett.*, 2009, **95**, 123105.
  - <sup>28</sup> J. M. Pruneda, Origin of half-semimetallicity induced at interfaces of C-BN heterostructures, *Phys. Rev. B*, 2010, **81**, 161409(R).
  - <sup>29</sup> G. S. Seal and J. Guo, Bandgap opening in boron nitride confined armchair graphene nanoribbon, *Appl. Phys. Lett.*, 2011, **98**, 143107.
  - <sup>30</sup> S. Jungthawan, S. Limpijumngong and J. L. Kuo, Electronic structures of graphene/boron nitride sheet superlattices, *Phys. Rev. B*, 2011, **84**, 235424.
  - <sup>31</sup> D. P. Gorony, M. Ebrahimi, F. Rosi, Arramel, Y. Fang, S. De Feyyer, C. Wang, P. H. Beton, A. T. S. Wee, P. S. Weiss and D. F. Perepichka, Supramolecular Assemblies on Surfaces: Nanopatterning, Functionality and Reactivity, *ACS Nano*, 2018, **12**, 7445.
  - <sup>32</sup> M. P. Levendorf, C. J. Kim, L. Brown, P. Y. Huang, R. W. Havener, D. A. Muller and J. Park, Graphene and boron nitride lateral heterostructures for atomically thin circuitry, *Nature*, 2012, **488**, 627.
  - <sup>33</sup> L. X. Chen, L. He, H. S. Wang, H. M. Wang, S. J. Tang, C. X. Cong, H. Xie, L. Li, H. Xia, and T. X. Li, Oriented graphene nanoribbons embedded in hexagonal boron ni-

- tride trenches, *Nat. Commun.*, 2017, **8**, 14703.
- <sup>34</sup> H. S. Wang, L. X. Chen, K. Elibol, L. He, H. M. Wang, C. Chen, C. X. Jiang, C. Li, T. R. Wu, and C. X. Cong, Towards chirality control of graphene nanoribbons embedded in hexagonal boron nitride, *Nat. Mater.*, 2021, **20**, 202.
- <sup>35</sup> D. C. Geng, I. Abdelwahab, X. F. Xiao, A. Cernescu, W. Fu, V. Giannini, S. A. Maier, L. Li, W. P. Hu, and K. P. Loh, One-Pot Confined Epitaxial Growth of 2D Heterostructure Arrays, *ACS. Materials Lett.*, 2021, **3**, 217.
- <sup>36</sup> David M. T. Kuo, Charge transport through the multiple end zigzag edge states of armchair graphene nanoribbons and heterojunctions, *RSC Adv.*, 2024, **14**, 20113.
- <sup>37</sup> David M. T. Kuo, Topological states in finite graphene nanoribbons tuned by electric fields, *J. Phys.: Condens. Matter*, 2025, **37**, 085304.
- <sup>38</sup> David M. T. Kuo, Temperature-stable tunneling current in serial double quantum dots: insights from nonequilibrium green functions and Pauli spin blockade, *Phys. Chem. Chem. Phys.*, 2025, **27**, 5238.
- <sup>39</sup> E. Leobandung, L. J. Guo, Y. Wang and S. Y. Chou, Observation of quantum effects and Coulomb blockade in silicon quantum-dot transistors at temperatures over 100 K, *Appl. Phys. Lett.*, 1995, **67**, 938.
- <sup>40</sup> L. Zhuang, L. J. Guo and S. Y. Chou, Silicon single-electron quantum-dot transistor switch operating at room temperature, *Appl. Phys. Lett.*, 1998, **72**, 1205.
- <sup>41</sup> D. Loss and D. P. DiVincenzo, Quantum computation with quantum dots, *Phys. Rev. A*, 1998, **57**, 120.
- <sup>42</sup> C. H. Bennett and D. P. DiVincenzo, Quantum information and computation, *Nature*, 2000, **404**, 247.
- <sup>43</sup> David M. T. Kuo and Y. C. Chang, Tunneling Current Spectroscopy of a Nanostructure Junction Involving Multiple Energy Levels, *Phys. Rev. Lett.*, 2007, **99**, 086803.